An International Journal of Optimization and Control: Theories & Applications
ISSN: 2146-0957 eISSN: 2146-5703
Vol.16, No.4, pp.1514-1530 (2026)
https://doi.org/10.36922/IJOCTA026150060

RESEARCH ARTICLE

Hierarchical rule-based control of BESS for voltage regulation and ramp-rate smoothing in low-voltage networks with high photovoltaic

Thanh Ngo Ngoc*

Faculty of Information Technology, Electric Power University, Hanoi, Vietnam
thanhnn_cntt@epu.edu.vn

ARTICLE INFO

Article history:
Received: April 11, 2026
Revised: June 4, 2026
Accepted: June 8, 2026
Published Online: July 3, 2026

Keywords:
Battery energy storage system
Voltage regulation
Ramp-rate smoothing
Hierarchical control
Low-voltage distribution network

AMS Classification 2010:
90B50, 90C90

ABSTRACT

This study proposes a rule-based hierarchical control algorithm for a battery energy storage system (BESS) to simultaneously address two technical challenges in low-voltage distribution networks with high photovoltaic penetration: overvoltage/undervoltage at network nodes and violations of the power ramp-rate limit at the point of common coupling. The algorithm employs the linearized LinDistFlow power-flow model on a 4-bus radial feeder based on the International Council on Large Electric Systems (CIGRE) benchmark, with a 2,000 kWh/300 kW lithium iron phosphate BESS. The operating mechanism consists of two priority levels: Level 1, an inner loop converging from zero to determine the minimum charging/discharging power required to keep the terminal-node voltage within the permissible range; Level 2, an additional ramp-rate correction applied only when it has the same sign as the voltage command. The 24-h quasi-static simulation results show that the proposed algorithm (Scenario B) reduces the voltage deviation index by 38.66% relative to the no-BESS scenario (Scenario A), completely eliminates voltage violations from 2.8% to 0%, reduces the ramp-rate violation rate from 39.13% to 13.04%, decreases losses by 41.57%, and yields a state of charge drift of only −1.8%. Compared with the single-objective droop scenario (Scenario C), the proposed algorithm outperforms it in all evaluation metrics, confirming the effectiveness of the hierarchical mechanism with a minimum-charge inner loop in preserving battery capacity for coordinated grid services.

(cc) BY

1. Introduction

The rapid growth of distributed rooftop photovoltaic (PV) systems in low-voltage (LV) distribution networks has created serious technical challenges in voltage quality and power stability at the point of common coupling (PCC). When PV penetration exceeds 100% of peak load, reverse power flow can cause overvoltage on feeder sections with the high R/X ratio typical of LV networks.[1] Bueno-López *et al.*[2] indicated that voltage fluctuations in LV networks with high PV penetration may lead to system instability. Variations in solar irradiance cause power ramp-rates that exceed the permissible limit at the PCC.[3] The maximum ramp magnitude depends on the PV system size and the frequency of cloud-induced fluctuations.[4] The EN 50160:2010+A3:2019 standard specifies a permissible voltage range of ±10% relative to the nominal voltage under normal operating conditions.[5] IEEE 1547-2018 establishes grid-support functional requirements for distributed inverters, including Volt-Watt and Volt-VAr functions.[6] Khalil *et al.*[7] confirmed that the optimal size and location of PV combined with a battery energy storage system (BESS) directly affect voltage stability in distribution networks. Yang *et al.*[8] showed that fair active power management is necessary to ensure voltage security in grids with high PV penetration. Shafiullah

*Corresponding Author

et al.[9] provided a comprehensive review of PV grid-integration challenges, including voltage rise, power-quality degradation, and mitigation strategies based on BESS and smart inverters.

Battery energy storage systems have been identified as a key solution to these two challenges. Stecca *et al.*[10] presented a comprehensive review of BESS integration into distribution grids, including voltage regulation, frequency support, and power management services. Zhang *et al.*[11] proposed a stable voltage regulation method that minimizes PV curtailment. Nakamura *et al.*[12] developed an advanced voltage-control method for LV grids that coordinates BESS with PV inverters. Rezaei and Esmaeili[13] proposed a two-level coordinated control method for PV-BESS systems in unbalanced LV grids. Zhao *et al.*[14] designed a distributed BESS control scheme for voltage regulation at the transmission-distribution interface.

Lithium iron phosphate (LFP) batteries exhibit a characteristically flat voltage profile, which has important implications for control-loop design. Community-scale BESSs based on $LiFePO_4$ (LFP) chemistry are preferred for safety, cycle life, and cost, yet exhibit an open-circuit voltage–state-of-charge (OCV–SOC) curve that is nearly flat ($\approx$3.20–3.30 V/cell) over the operating window 20–80 % SOC, which makes voltage-based SOC estimation intrinsically more challenging than for nickel–manganese–cobalt chemistries.[15,16] Recent reviews on LFP/lithium-ion battery safety mechanisms, crosstalk mitigation, and hierarchical coordination highlight that robust control must simultaneously preserve priority ordering among competing stress factors and avoid drifting into extreme SOC regions.[15–17] The proposed algorithm explicitly mitigates these issues: (i) SOC is maintained by Coulomb counting through **Equations 10** and **11**, not by OCV inversion, so the flatness of the LFP voltage profile does not propagate into the SOC estimate; (ii) the inner loop regulates the grid-side terminal-node voltage—the BESS cell voltage is decoupled from the control objective; (iii) the under-relaxation factor $\beta = 0.4$ damps voltage-sensor noise and guarantees monotonic convergence;[14] and (iv) the soft SOC taper together with the V-floor restoration keep operation away from the extreme SOC regions where LFP voltage becomes nonlinear and noise sensitivity grows.

The challenge of managing two competing control objectives through a strict priority hierarchy finds conceptual analogs beyond power systems. In electrochemical engineering, Han *et al.*[18] recently demonstrated that competing interfacial reactions at zinc (Zn)-metal anodes can be hierarchically regulated through a multi-coordination molecular dynamic bridging strategy:[18] a tris(2-pyridylmethyl)amine (TPA) additive with four N-atom coordination sites dynamically prioritizes Zn^{2+} solvation (primary process, analogous to priority-1 voltage regulation) while simultaneously facilitating trifluoromethanesulfonate anion decomposition (secondary, cooperative process, analogous to the additive ramp-smoothing correction applied only when cooperative with the voltage outcome). This multi-coordination-molecular-bridging strategy achieves hierarchical control of competing reactions, forming a robust solid–electrolyte interphase over more than 4,000 cycles with 81.9% capacity retention. An analogous hierarchical coordination principle underpins the proposed BESS algorithm: inner-loop voltage regulation is always resolved first, after which ramp-smoothing correction is applied additively only when consistent with the voltage outcome, ensuring that regulatory compliance is never sacrificed for ramp performance.[15–17]

Regarding smart inverter functional control, Xu *et al.*[19] provided a comprehensive review of grid-support functions, including Volt-Watt and Volt-VAr, under IEEE 1547-2018.[6] Inaolaji *et al.*[20] optimized Volt-VAr and Volt-Watt droop settings in unbalanced multiphase networks. Chathurangi *et al.*[21] systematically compared Volt-VAr, Volt-Watt, and combined strategies to maximize PV hosting capacity. Archetti *et al.*[22] conducted hardware-in-the-loop validation for Volt-Watt and Volt-VAr control in distribution systems with distributed renewable energy sources. Carlak and Güler[23] designed an inverter control algorithm that combines Volt/VAr functionality with demand management. Yousefi *et al.*[24] employed stochastic distributed optimization with reactive power support for voltage control in high-PV-penetration grids.

Regarding BESS solutions for ramp-rate smoothing, Atif and Khalid[25] applied a Savitzky–Golay filter combined with BESS to achieve ramp-rate compliance. Syed and Khalid[26] proposed a moving-regression filter with SOC feedback for PV ramp-rate mitigation. Abdalla *et al.*[27] developed an adaptive smoothing strategy that dynamically adjusts the filter time constant based on PV variability and the SOC of hybrid storage. Hossain *et al.*[28] presented a compensation strategy using a multilevel hybrid energy storage system, consisting of batteries and supercapacitors, to mitigate PV fluctuations in microgrids. Abdalla *et al.*[29] designed a monotonic charging controller for parallel-connected BESS units to reduce the ramp rate while mitigating battery aging. Makibar *et al.*[30] proposed a battery downsizing method for PV ramp-rate control. Ryu *et al.*[31] used short-term PV forecasting based on sky images for predictive battery smoothing control. Cano *et al.*[32] compared hybrid battery-supercapacitor configurations for PV power smoothing through simulation and experiments.

However, most of the above studies treat voltage regulation and ramp-rate smoothing as two separate objectives. When combined, fixed-weight approaches often create conflicts between the two objectives, leading to early SOC depletion and reduced control effectiveness in the evening, when the load increases.[33] Bektaş *et al.*[33] indicated that integrated energy management in distribution grids with PV and BESS requires a coordination mechanism among multiple devices. Kumar and Kumar[34] showed that battery aging cost increases significantly when BESS multi-objective operation lacks prioritization. Zakaria *et al.*[35] performed multi-objective optimization of PV, BESS, and capacitor banks in LV grids, yet did not establish a clear hierarchy between voltage and ramp. Emarati *et al.*[36] proposed a two-level overvoltage control strategy but did not consider the ramp rate. Khan *et al.*[37] coordinated the on-load tap changer and BESS to mitigate voltage fluctuations, yet lacked a clear prioritization mechanism between voltage and ramp. López *et al.*[38] analyzed the impact of PV-BESS strategies on LV grids, yet did not simultaneously optimize both objectives.

Regarding hierarchical control, Fahad *et al.*[39] presented a hierarchical control scheme for demand management in active distribution networks. Mohamed *et al.*[40] developed a three-level hierarchical controller for EV charging stations integrated with PV and BESS. Nguyen[41] investigated coordinated demand management and energy storage for a hybrid PV-wind microgrid, achieving a 96.49% reduction in electricity cost through optimal scheduling. Demirtas and Ahmad[42] presented a particle swarm optimization-optimized fractional fuzzy proportional–integral controller for power factor improvement. Perin *et al.*[43] used a swarm optimization algorithm to design generator rotors.

Regarding linear power-flow models for distribution networks, Patari *et al.*[44] reviewed distributed optimization methods based on the LinDistFlow approximation. Zhang *et al.*[45] proposed distributed voltage-constrained optimization in integrated primary-secondary distribution systems using a linearized power-flow approximation. Paudel *et al.*[46] developed a decentralized energy trading mechanism that incorporates voltage constraints using the LinDistFlow model. Montoya *et al.*[47] proposed a second-order convex approximation of the power-flow equations for optimal BESS operation.

With respect to SOC management and battery lifetime, Jamroen[48] investigated the impact of SOC management strategies on the economic effectiveness of BESS for voltage regulation. Gräf *et al.*[49] analyzed the factors causing capacity degradation in utility-scale BESS, showing that operating strategy and temperature are the two main factors.

Regarding community battery storage, Hupez *et al.*[50] proposed a cooperative framework for fair resource allocation and cost optimization in LV energy communities. Jouttijärvi *et al.*[51] evaluated the techno-economic feasibility of a community direct current (DC) PV-battery system with shared energy exchange.

From the above review, the research gap is identified as follows: there is still a lack of a rule-based control algorithm that is sufficiently simple for real-time implementation, provides a clear hierarchical priority mechanism between voltage and ramp-rate, and minimizes the charging/discharging power required for voltage regulation in order to preserve SOC for ramp-smoothing service and evening discharge. This study proposes a rule-based hierarchical control algorithm with an inner loop converging from zero to address this gap, and validates it through a 24-h quasi-static simulation on a 4-bus CIGRE feeder with a 2,000 kWh/300 kW community LFP BESS.

2. Methodology

A 4-bus radial LV distribution network model (Bus 1 to Bus 4) was constructed according to the CIGRE TF C6.04.02 benchmark, using NFA2X 4×150 mm^2 cable with the following technical parameters: unit resistance $r = 0.206\ \Omega/km$, unit reactance $x = 0.074\ \Omega/km$.[10,13] The base system consists of a base voltage $V_{\text{base}} = 0.4$ kV and a base power $S_{\text{base}} = 1$ MVA, from which the base impedance is obtained as in **Equation 1**.

$$Z_{\text{base}} = \frac{V_{\text{base}}^2}{S_{\text{base}}} = 0.16\ \Omega \tag{1}$$

The branch lengths are $L_{12} = 55$ m, $L_{23} = 50$ m, and $L_{34} = 45$ m (total 150 m). The per-unit resistance and reactance of each branch are given by **Equation 2**.

$$R_{\text{pu},i} = \frac{r \cdot L_i}{Z_{\text{base}}}, X_{\text{pu},i} = \frac{x \cdot L_i}{Z_{\text{base}}} \tag{2}$$

where $i \in \{12,\ 23,\ 34\}$. The total resistance is $R_{\text{sum}} = \sum R_{\text{pu},i} = 0.1931$ pu. The ratio $\frac{R}{X} = 2.78$ characterizes the resistance-dominant nature of LV networks.[1,44]

The power-flow analysis uses the linearized LinDistFlow model, neglecting the second-order loss term.[1,46] For node $k = \{1, 2, 3\}$on the radial feeder, with node 0 as the slack bus ($V_0 = 1.0$ pu), the linear voltage equation is expressed as in **Equation 3**.

$$V_k = V_{k-1} - R_{\text{pu},k} P_{k-1,k} - X_{\text{pu},k} Q_{k-1,k} \tag{3}$$

where V_k is the voltage at node k(pu), and $P_{k-1,k}$ and $Q_{k-1,k}$ are the active and reactive power flows on the branch $(k-1, k)$, respectively (pu). The branch power flows are determined from nodal power balance, as given in **Equations 4** and **5**.

$$P_{k-1,k} = p_k + P_{k,k+1} \tag{4}$$

$$Q_{k-1,k} = q_k + Q_{k,k+1} \tag{5}$$

where p_k and q_k are the net active and reactive power consumptions at node k. At the terminal node (Bus 4 in the model, i.e., node 3 counted from 0), $P_{3,4} = p_3$ and $Q_{3,4} = q_3$. The voltage sensitivity with respect to active power is given in **Equation 6**.

$$\frac{\partial V_3}{\partial P} = \frac{R_{\text{sum}}}{S_{\text{base}}} = 1.931 \times 10^{-4} \text{ pu/kW} \tag{6}$$

The load demand is uniformly distributed over the three load buses (Buses 2, 3, and 4), with a total peak load and a power factor. The hourly load profile uses the standard H0 curve from the Open Power System Data project,[52] with added Gaussian noise to represent micro-level randomness. $P_{\text{peak}} = 400$ kW, $\cos\varphi = 0.95, and\ \sigma = 0.03$

The PV power is modeled using a Gaussian clear-sky profile,[7] as in **Equation 7**.

$$P_{\text{pv}}(t) = P_{\text{rated}} \cdot \exp - \frac{(t-t_{\text{pk}})^2}{2\sigma_{\text{pv}}^2} \cdot f_{\text{derate}}(t) \tag{7}$$

where $P_{\text{rated}} = 600$ kWp, $t_{\text{pk}} = 12$ h is the irradiance peak time, and $\sigma_{\text{pv}} = 3.5$ h is the profile width. The nominal operating cell temperature (NOCT)-based thermal derating factor (IEC 61215) is described by **Equations 8** and **9**, with $T_{\text{amb}} = 27\,°\text{C}$, NOCT $= 45\,°\text{C}$, $\gamma_{\text{tc}} = -0.004/°\text{C}$, and $G_{\text{ref}} = 1000$ W/m^2.

$$f_{\text{derate}}(t) = 1 + \gamma_{\text{tc}} \cdot (T_{\text{cell}}(t) - 25 \tag{8}$$

$$T_{\text{cell}}(t) = T_{\text{amb}} + (\text{NOCT} - 20) \cdot \frac{G_{\text{POA}}(t)}{G_{\text{ref}}} \tag{9}$$

A community LFP BESS[50,51] is considered, with an energy capacity $E_{\text{cap}} = 2,000$ kWh, maximum charging/discharging power $P_{\text{ch,max}} = P_{\text{dis,max}} = 300$ kW (C-rate $= 0.15C$), charging efficiency $\eta_c = 0.96$, and discharging efficiency $\eta_d = 0.96$.[45] The allowable SOC range is $SOC_{\min} = 20\%$, $SOC_{\max} = 80\%$. The usable energy capacity is $E_{\text{usable}} = (SOC_{\max} - SOC_{\min}) \cdot E_{\text{cap}} = 1,200$ kWh.

The discrete SOC dynamics are described by **Equations 10** and **11**, where $P_B(k)$ is the BESS power at the time step k(kW), positive for charging and negative for discharging, and $\Delta t = 1$ h.

$$SOC(k+1) = SOC(k) + \frac{P_B(k) \cdot \Delta t \cdot \eta_c}{E_{\text{cap}}},$$

if $P_B(k) \geq 0$ (10)

$$OC(k+1) = SOC(k) + \frac{P_B(k) \cdot \Delta t}{E_{\text{cap}} \cdot \eta_d},$$

if $P_B(k) < 0$ (11)

The hierarchical control algorithm consists of five steps at each time step $k = 1, \ldots, 24$:

(i) Step 1: Inner voltage-convergence loop from zero: Initialize $B_v = 0$. Iterate for at most $N_{\max} = 15$ times. Compute $V_3(B_v)$ from LinDistFlow according to previous **Equations 3–5**. If $V_3 > V_{hi,db}$, then **Equation 12** applies.

$$B_v \leftarrow \min(B_v + \beta \cdot k_v \cdot (V_3 - V_{hi,db}),\ P_{ch,\max}) \tag{12}$$

If $V_3 < V_{lo,db}$, then **Equation 13** applies.

$$B_v \leftarrow \max(B_v - \beta \cdot k_v \cdot (V_{lo,db} - V_3), \\ -P_{dis,\max}) \tag{13}$$

Otherwise, stop the iteration.

Here, $V_{hi,db} = 1.03\ pu; V_{lo,db} = 0.97\ pu$ are the deadband activation thresholds. $k_v = P_{\text{ch,max}}/(V_{\text{hi}} - V_{\text{hi,db}}) = 10,000$ kW/pu is the droop slope. $\beta = 0.40$ is the under-relaxation factor. The SOC constraint is applied at each iteration as in **Equations 14** and **15**.

$$B_v \leftarrow \min\left(B_v,\ \frac{(SOC_{\max} - SOC(k)) \cdot E_{cap}}{\eta_c \cdot \Delta t}\right),$$

if $B_v > 0$ (14)

$$B_v \leftarrow \max\left(B_v,\ -\frac{(SOC(k) - SOC_{\min}) \cdot E_{cap} \cdot \eta_d}{\Delta t}\right),$$

if $B_v < 0$ (15)

The effective open-loop gain is $G_{eff} = \beta \cdot k_v \cdot \partial V_3/\partial P$. With $\beta = 0.40$, $k_v = 10,000\ kW/pu$, $\partial V_3/\partial P = 1.931 \times 10^{-4}\ pu/kW$, one obtains $G_{eff} = 0.40 \times 10,000 \times 1.931 \times 10^{-4} = 0.77 < 1$.

The condition guarantees monotonic convergence according to the Lyapunov criterion for a discrete linear feedback system.[14] In particular, the loop is initialized from and converges upward, meaning that only the minimum charging/discharging amount required to place the voltage inside the deadband is determined, thereby preserving the SOC capacity to the greatest extent for other objectives. $G_{eff} < 1 B_v = 0$

(ii) Step 2: Ramp-rate prediction: After voltage convergence, the PCC power after voltage correction, P_{net,B_v}, is calculated, and the predicted ramp is obtained as in **Equation 16**.

$$r_{pred}(k) = P_{net,B_v}(k) - P_{net,B}(k-1) \quad (16)$$

The ramp-correction amount is determined by **Equations 17–19**, where $RL = 0.10 \cdot P_{rated} = 60\ kW/h$ is the ramp-rate limit.[6]

$$B_r = -(r_{pred} - RL), \text{if } r_{pred} > RL \quad (17)$$

$$B_r = -(r_{pred} + RL), \text{if } r_{pred} < -RL \quad (18)$$

$$B_r = 0, \text{if } \mid r_{pred} \mid \leq RL \quad (19)$$

(iii) Step 3: Hierarchical combination: The combination statement for the two components follows the rules in **Equations 20–22**.

$$\text{If } B_v = 0 : B_{ctrl} = B_r \quad (20)$$

$$\text{If } sign(B_v) = sign(B_r) : B_{ctrl} = B_v + B_r \quad (21)$$

$$\text{If } sign(B_v) \neq sign(B_r) : B_{ctrl} = B_v \quad (22)$$

Equation 22 guarantees absolute priority for voltage when the two objectives conflict, preventing the case where the BESS discharges to reduce ramp while causing overvoltage, or charges to reduce ramp while causing undervoltage.[19,29]

(iv) Step 4: Soft SOC taper and V-floor restoration: When the SOC approaches the limits, a linear reduction factor is applied as in **Equations 23** and **24**, where $SOC_{soft,\min} = SOC_{\min} + \Delta SOC = 0.35$, $SOC_{soft,\max} = SOC_{\max} - \Delta SOC = 0.65$, and $\Delta SOC = 0.15$ is the taper margin. The taper factor is defined as $\alpha_{chg} = clip\left(0.5\frac{SOC_{\max} - SOC}{\Delta_{taper}}, 0, 1\right)$ when charging and $\alpha_{dis} = clip\left(0.5\frac{SOC - SOC_{\min}}{\Delta_{taper}}, 0, 1\right)$ when discharging, with $\Delta_{taper} = 0.15$.

$$\text{If } B_{ctrl} < 0 \text{ and } SOC < SOC_{soft,\min} : B_{ctrl} \leftarrow B_{ctrl} \cdot \max\left(0, \frac{SOC - SOC_{\min}}{\Delta SOC}\right) \quad (23)$$

$$\text{If } B_{ctrl} > 0 \text{ and } SOC > SOC_{soft,\max} : B_{ctrl} \leftarrow B_{ctrl} \cdot \max\left(0, \frac{SOC_{\max} - SOC}{\Delta SOC}\right) \quad (24)$$

After tapering, the voltage component is restored to its floor (V-floor restoration) via **Equations 25** and **26**, ensuring that tapering reduces only the ramp component and never the voltage component, thereby maintaining voltage compliance even when the SOC is close to its limits.

$$\text{If } B_v > 0 : B_{ctrl} \leftarrow \max(B_{ctrl}, B_v) \quad (25)$$

$$\text{If } B_v < 0 : B_{ctrl} \leftarrow \min(B_{ctrl}, B_v) \quad (26)$$

(v) Step 5: Hard SOC constraint and power limit: These are enforced by **Equations 27** and **28**.

$$B_{ctrl} \leftarrow clamp(B_{ctrl}, B_{SOC,\min}, B_{SOC,\max}) \quad (27)$$

$$B_{ctrl} \leftarrow clamp(B_{ctrl}, -P_{dis,\max}, P_{ch,\max}) \quad (28)$$

The loss on each branch is calculated by the quadratic approximation. The total energy loss over 24 h is given by **Equations 29** and **30**.

$$P_{loss,i} = R_{pu,i} \cdot \frac{P_{i-1,i}^2}{V_i^2} \quad (29)$$

$$E_{loss} = \sum_{k=1}^{24} \sum_{i=1}^{3} P_{loss,i}(k) \cdot \Delta t \quad (30)$$

The performance indices are defined as follows:[6,11,21]:

The mean voltage deviation index (VDI) is defined by **Equation 31**, where $N = 3$ load buses and $T = 24$ time steps.

$$VDI = \frac{1}{NT} \sum_{k=1}^{T} \sum_{n=1}^{N} \mid V_n(k) - 1 \mid \quad (31)$$

The voltage violation rate (VVR) and the ramp-rate violation rate (RRV) are defined by **Equations 32** and **33**, where $\Delta P_{PCC}(k) = P_{PCC}(k) - P_{PCC}(k-1)$.

$$VVR = \frac{1}{NT} \sum \mathbf{1}(V_n(k) < V_{lo} \vee V_n(k) > V_{hi}) \cdot 100\% \quad (32)$$

$$RRV = \frac{1}{T-1} \sum_{k=2}^{T} \mathbf{1}(\mid \Delta P_{PCC}(k) \mid > RL) \cdot 100\% \quad (33)$$

The SOC drift and the equivalent cycle count are calculated by **Equations 34** and **35**, where $E_{thru} = \sum \mid P_B(k) \mid \cdot \Delta t$ is the total processed energy.

$$\delta SOC = SOC(T) - SOC \quad (34)$$

$$N_{cyc} = \frac{E_{thru}}{2 \cdot E_{cap}} \tag{35}$$

The simulation was carried out in quasi-static form over 24 h with a time step $\Delta t = 1\ h$, comparing three scenarios: A (without BESS as the baseline), B (the proposed hierarchical $V+R$ algorithm), and C (voltage droop only, using the same inner loop from zero but without Step 2 and Step 3). Sensitivity analysis was performed over the parameter space $k_v \times RL$.

3. Results and discussion

Figure 1 presents the 24-h PV and load profiles. The PV power peaks at 535 kW at h12, whereas the load peaks at 404 kW at h19. The PV penetration-to-peak-load ratio reaches 150%, resulting in pronounced reverse power flow during h8–h15.

Table 1 presents the voltage-performance results. Scenario A (without BESS) has $VDI = 0.02163$ pu with $VVR = 2.8\%$. The maximum voltage at Bus 4 reaches 1.0654 pu, exceeding the threshold $V_{hi,db} = 1.03$ pu. The minimum voltage reaches 0.9538 pu, below $V_{lo,db} = 0.97$ pu. The proposed algorithm (B) reduces VDI to 0.01327 pu, corresponding to an improvement of 38.66%, and completely eliminates voltage violations. The single-objective droop scenario (C) achieves $VDI = 0.01494$ pu, corresponding to an improvement of 30.94%. It also eliminates voltage violations, yet with lower effectiveness than Scenario B.

Figure 2 illustrates the hourly voltage profile at Bus 4. Curve A (blue dashed line) exceeds $V_{hi,db}$during h10–h14 and falls below $V_{lo,db}$ during h19–h20. Curve B (solid red line) is controlled within the range (0.97, 1.03) pu, except at h14 when the SOC reaches 80% and the algorithm switches to taper mode. Curve C (green dash-dot line) also remains within the deadband range, yet its evening voltage drops faster than that of B because of early SOC depletion.

Figure 3 presents the voltages at all three load buses (Buses 2, 3, and 4), showing the shaded improvement region between A and B. The voltage improvement increases progressively from Bus 2 to Bus 4 because of the cumulative impedance effect along the radial feeder.

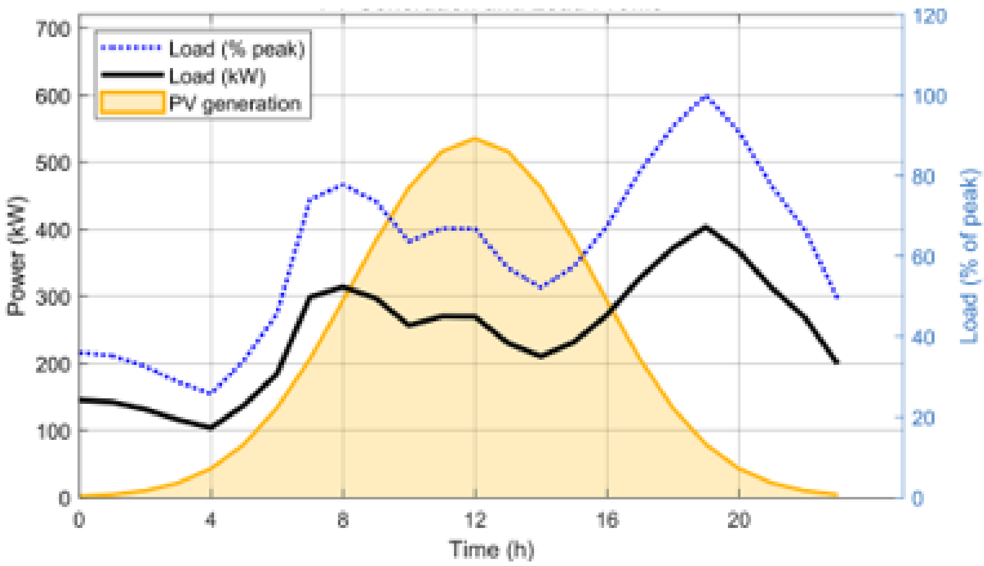

Figure 1. 24-h PV generation and load demand profiles

Table 1. Voltage performance

Metric	Scenario A	Scenario B	Scenario C
VDI_MA (pu)	0.02163	0.01327	0.01494
VDI_RMS (pu)	0.02690	0.01675	0.01815
VDI improvement (%)	0.00	38.66	30.94
VVR (%)	2.8	0.0	0.0
$V_{\max}$ at Bus 4	1.0654	1.0458	1.0396
$V_{\min}$ at Bus 4	0.9538	0.9700	0.9700

Abbreviations: VDI_MA: Mean absolute voltage deviation index; VDI_RMS: Root mean square voltage deviation index; VVR: Voltage violation rate.

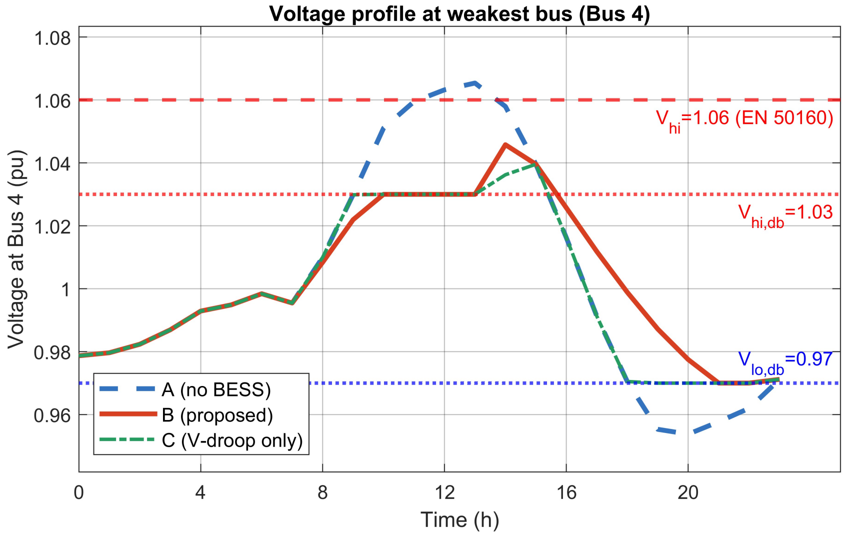

Figure 2. Terminal bus (Bus 4) voltage profile over 24 h for Scenarios A, B, and C

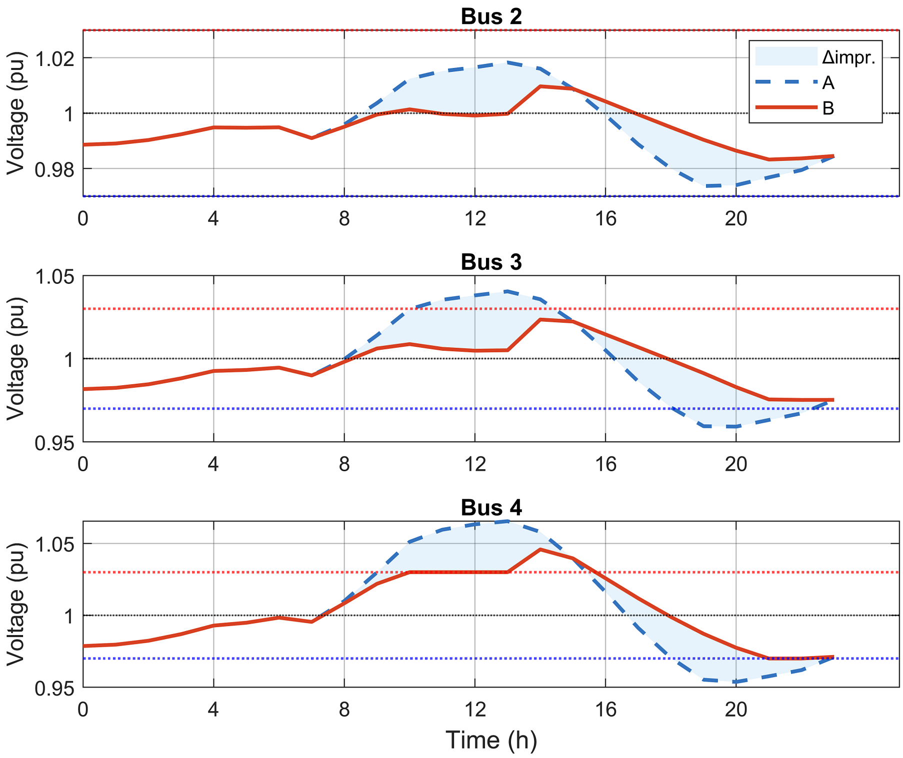

Figure 3. Voltage profiles at load buses 2–4 for scenarios A and B with improvement region hours for Scenarios A, B, and C

Table 2 presents the ramp-rate performance. Scenario A has a maximum | *ramp* |of 141.9 kW/h with $RRV = 39.13\%$, that is, 9/23 time steps exceed the 60 kW/h limit. The proposed algorithm (B) reduces the maximum | *ramp* | to 137.8 kW/h and reduces RRV to 13.04%, corresponding to a 66.7% reduction in the number of violations relative to A. The mean ramp decreases from 54.4 kW/h in A to 35.4 kW/h in B, corresponding to a 34.9% reduction. Scenario C maintains $RRV = 30.43\%$and leaves the maximum | *ramp* |unchanged at 141.9 kW/h. It does not improve the ramp because it lacks a correction mechanism.

Figure 4 consists of two plots: (A) PCC power and (B) hourly ramp-rate. Plot (A) shows that B significantly flattens the PCC profile relative to A, reducing the maximum reverse-power-flow magnitude from −280 kW to −130 kW. Plot (B) shows that the ramp-rate of B (red squares) lies mainly within the band ±60 kW/h, whereas A (blue bars) and C (green triangles) exceed the limit multiple times.

Table 2. Ramp-rate performance

Metric	Scenario A	Scenario B	Scenario C
Max |ramp| (kW/h)	141.9	137.8	141.9
RRV (%)	39.13	13.04	30.43
Mean |ramp| (kW/h)	54.4	35.4	41.1

Abbreviation: RRV: Ramp-rate violation rate.

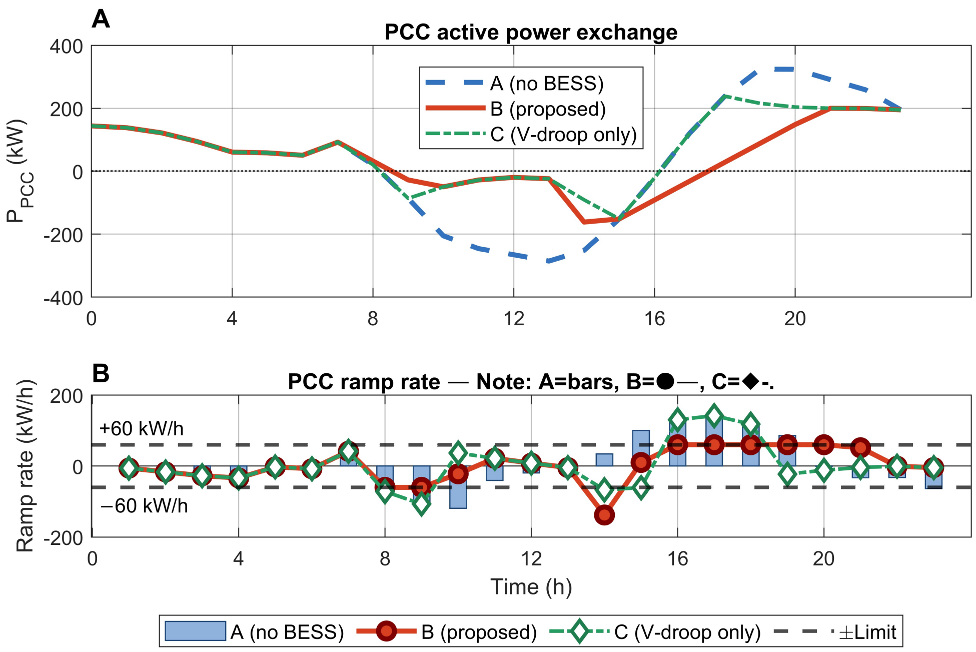

Figure 4. (A) PCC active power and (B) ramp-rate profiles over 24 h for scenarios A, B, and C. Abbreviations: BESS: Battery energy storage system; PCC: Point of common coupling

Table 3. BESS operation

Metric	Scenario B	Scenario C
Initial SOC (%)	30.0	30.0
Final SOC (%)	28.2	60.3
SOC min (%)	28.2	30.0
SOC max (%)	80.0	80.0
Throughput (kWh)	2035.5	1420.6
Equivalent cycles	0.509	0.355
Peak charge (kW)	261.7	261.6
Peak discharge (kW)	235.8	120.0
SOC drift (%)	−1.8	+30.3

Abbreviations: BESS: Battery energy storage system; SOC: State-of-charge.

Table 3 presents the BESS operating performance. The SOC of B starts at 30%, reaches a maximum of 80% at h14, then discharges steadily to 28.2%; the SOC drift is only −1.8%, which is nearly energy-neutral. Scenario C has an SOC drift of +30.3%, from 30% to 60.3%, showing that the single-objective droop only charges and lacks an active evening discharge mechanism.

Figure 5 consists of two plots: (A) BESS power and (B) hourly SOC. Plot (A) shows that B charges during h8–h14 (red region) and discharges during h16–h22 (blue region), whereas C (black dashed line) only discharges during h16–h22 with a much smaller magnitude. Plot (B) shows that the SOC trajectory of B (thick solid red line) exhibits a nearly perfectly symmetric charge-discharge pattern, whereas C (green dashed line) ends at 60%, which is not sustainable for multi-day operation. Expected BESS service life under the proposed strategy. $E_{th,day} = 2,035\ kWh, E_{rated} = 2,000\ kWh$; $N_{EFC,day} = \frac{E_{th,day}}{E_{rated}} = \frac{2035}{2000} = 1.0175\ EFC/day$; $N_{EFC,year} \approx 186\ EFC/year$, with the LFP cycle-life specification $N_{EFC,80\%SOH} = 2,500\text{–}4,000\ EFC$, the cycle-limited service life is estimated as $T_{cycle} = \frac{N_{EFC,80\%SOH}}{N_{EFC,year}} = \frac{2,500\text{–}4,000}{186} \approx 13.4\text{–}21.5\ years$. However, practical LFP operation is also constrained by calendar ageing, $T_{calendar} \approx 10\text{–}15\ years$, where degradation is mainly accelerated by high-SOC storage, electrolyte decomposition, and lithium plating. Therefore, the effective BESS service life under the proposed duty cycle is$T_{BESS} = \min\left(T_{cycle}, T_{calendar}\right) \approx 10\text{–}15\ years$. This result indicates that calendar aging, rather than cycling aging, is expected to be the dominant life-limiting mechanism. The proposed strategy supports this lifetime projection through $\lim_{t\to 0^+} C_{rate}(t)$ bounded due to the convergence-from-zero inner loop, and through $SOC(t) \approx \not{S}OC_{\max}$ due to the V-floor restoration mechanism, thereby reducing prolonged high-SOC dwell time where calendar aging is most severe.

Table 4 presents the energy balance. The total PV generation is 4,846.2 kWh/day. The total load is 5,864.7 kWh/day. The network losses decrease from 180.65 kWh in A to 105.56 kWh in B, corresponding to 41.57%. Scenario C reduces the losses by 38.10%, lower than B, because the PCC power profile still has a high amplitude during the evening load valley.

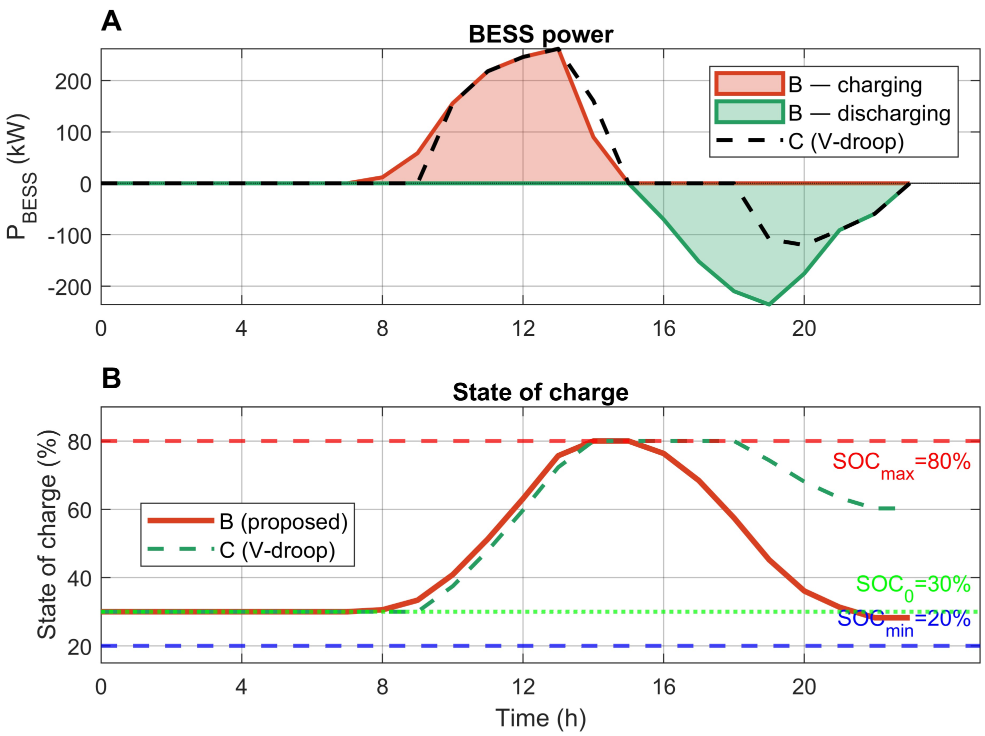

Figure 5. (A) Battery energy storage system (BESS) charge/discharge power and (B) state of charge (SOC) profiles for Scenarios B and C

Table 4. Energy balance

Metric	Scenario A	Scenario B	Scenario C
Photovoltaic energy generation (kWh)	4,846.2	4,846.2	4,846.2
Load (kWh)	5,864.7	5,864.7	5,864.7
Losses (kWh)	180.65	105.56	111.83
Loss reduction (%)	–	41.57	38.10

Figure 6 decomposes the BESS power into two components: P_v, the minimum charging/discharging power for voltage regulation, and P_r, the additional ramp correction. During the charging interval h8–h14, P_v is dominant. P_r only adds support at h8–h9 when the negative ramp is large. During the discharging interval h16–h22, both P_v and P_r contribute. P_r helps control the discharge rate under the 60 kW/hramp limit. The total P_{ctrl} (black line) is always equal to the sum of the two components, confirming the consistency of the decomposition algorithm.

Figure 7 shows the bar chart of the maximum voltage deviation at the three load buses for all three scenarios. Scenario A exceeds the 3% threshold at Bus 3 (4.1%) and Bus 4 (6.5%). Both B and C reduce the deviation at Bus 4 to below 5%. B (4.6%) remains higher than C (4.0%) at Bus 4 because B occasionally gives priority to ramp over voltage during cooperative intervals. Under the global metric, i.e., mean VDI, B remains superior.

Table 5 presents the sensitivity-analysis results over the parameter space $k_v \in \{2,000, 5,000, 10,000, 15,000\}, R_L \in \{30, 60, 90, 120\}$ kW/h. At $k_v = 2,000$ (weak droop), the VDI improvement is only 23%, yet RRV is low because the BESS intervention is limited. When $k_v$increases to $10,000$–$15,000$, the VDI improvement reaches 32%, yet RRV increases because V–R conflicts become more frequent. The limit $RL = 60$ kW/h provides the best trade-off: VDI improvement = 32%, $RRV = 13\%$, max $\mid ramp \mid = 114$ kW/h. The sensitivity table clearly separates the operating points. It confirms that the algorithm remains stable over a wide range of parameters.

Sensitivity to BESS-rated power is evaluated by $P_{ch,\max} = P_{dis,\max} = P_{\max} \in \{300, 600, 900, 1,200\}kW$, corresponding to $C_{rate} \in [0.15, 0.60]C$, while $E_{BESS} = 2,000kWh$, $k_v = 10,000kW/pu$, and $R_L = 60kW/h$ are fixed. The numerical sweep gives $VDI(P_{\max}) = const.$, $RRV(P_{\max}) = 13.0\%$, and unchanged ramp and SOC trajectories, because $P_{\max}$ is not the active constraint in this feeder: $P_{ch,peak} = 261.7kW < 300kW = P_{\max}$, $P_{ch,peak}/P_{\max} = 87.2\%$. Hence, the binding constraints are structural rather than inverter-rated: first, the LinDistFlow voltage correction reaches its feasible limit once $V_i(t) \in [V_{lo,db}, V_{hi,db}]$, so additional inverter headroom cannot further reduce voltage deviation; second, $SOC(t) \to SOC_{\max} = 0.80$at $t = 13h$, after which $P_{ch}(t) = 0$is enforced regardless of $P_{\max}$. The residual ramp violation occurs at $t = 14h$, where $P_V > 0$ and $P_R < 0$, meaning that the voltage-support command requests charging while the ramp-control command requests discharging; therefore, the cooperative logic imposes $P_{BESS} \neq P_V + P_R$ under opposite command signs, and the resulting PCC power step remains unavoidable at $\Delta t = 1h$. Consequently, increasing $P_{\max}$ from 300 to $1,200kW$ does not alter VDI, RRV, ramp statistics, or SOC feasibility. For the studied four-bus residential feeder with $P_{PV}^{\max} = 600kW$ and $P_{load}^{\max} = 400kW$, the control-performance right-sizing point is therefore $P_{\max}/E_{BESS} = 300/2,000 = 0.15C$; oversizing the inverter to $1,200kW$increases the power-electronics rating by $4\times$ without a measurable control benefit.

Figure 8 presents the radar chart of five normalized key performance indicators: VDI, VVR, ramp, loss, and BESS utilization. Scenario B (solid red line) encloses a larger area than C (blue dashed line) on every axis. The advantage is most pronounced on the BESS-utilization axis, due to a 43% higher throughput, and on the ramp axis, because C has no ramp-correction mechanism.

The key mechanism that gives the proposed algorithm (B) an advantage over the single-objective droop (C) lies in the convergence-from-zero loop (Step 1). Conventional droop computes the open-loop charging/discharging command as $P_B = k_v \cdot \Delta V$ and applies it directly.[19] The convergence-from-zero loop determines only the minimum charging/discharging amount required to drive the voltage into the deadband.[25] This creates the critical difference. During h10–h13, when overvoltage is severe, B charges only 155–262 kW, i.e., exactly the required level. C charges at the same level ($155 - 262$ kW) because both use the same inner loop. The difference appears in the discharge interval: B discharges 70–236 kW during h16–h20 because sufficient SOC remains available and the additional P_r term is active. C does not discharge actively. As a result, $SOC_C^{\text{final}} = 60.3\%$ which indicates surplus stored energy.

The under-relaxation factor plays a critical role in the convergence behavior. As shown in **Equation 17**, the iterative loop converges monotonically when an under-relaxation factor is applied.[14] In the absence of relaxation, the iterations may exhibit oscillatory behavior or diverge. The Lyapunov stability analysis confirms that the Lyapunov function decreases monotonically when[45] $\beta = 0.40,\ G_{eff} = 0.77 < 135,\ \beta = 1.0,\ G_{eff} = 1.93 > 1, V(k) = (V_3(k) - V_{ref})^2,\ and\ G_{eff} < 1.$

The V-floor restoration mechanism, given by **Equations 27** and **28**, resolves the SOC-taper issue while maintaining voltage compliance. When the SOC approaches 80% at h14, taper reduces B_{ctrl}. The V-floor guarantees that the B_v component is not reduced. Only the P_r component is affected. The result is $V_3 \leq 1.046$ pu at h14, which remains within the permissible range, while $P_r \rightarrow 0$ at that instant.

Applicability and operating envelope are characterized by $R/X \geq 2$, radial LV topology, and terminal-concentrated PV injection, with the principal sizing domain defined as $1.0 \leq P_{PV}^{\max}/P_{load}^{\max} \leq 2.0$. If $P_{PV}^{\max}/P_{load}^{\max} < 1.0$, overvoltage activation is rare, and the controller reduces to $P_{BESS} \approx P_R$; if $P_{PV}^{\max}/P_{load}^{\max} > 2.0$, $SOC(t) \rightarrow SOC_{\max}$ earlier, requiring either E_{BESS} ↑or P_{curt} ↑. Since Step 1 uses only terminal-node voltage feedback, $V_{term}(t)$, the control law is weakly dependent on the exact PV spatial distribution along the feeder. For irradiance-transient sites, the hourly RRV at $\Delta t = 1$is interpreted as a conservative lower-resolution estimate; the sub-hourly reassessment in **Table 6**, with $\Delta t = 5\,\text{min}$, $N = 288 steps/day$, Markov-chain cloud attenuation applied to the PV profile, and noisy interpolation applied to the load profile, confirms that the proposed algorithm retains its qualitative advantage over Scenario A at sub-hourly time scales.

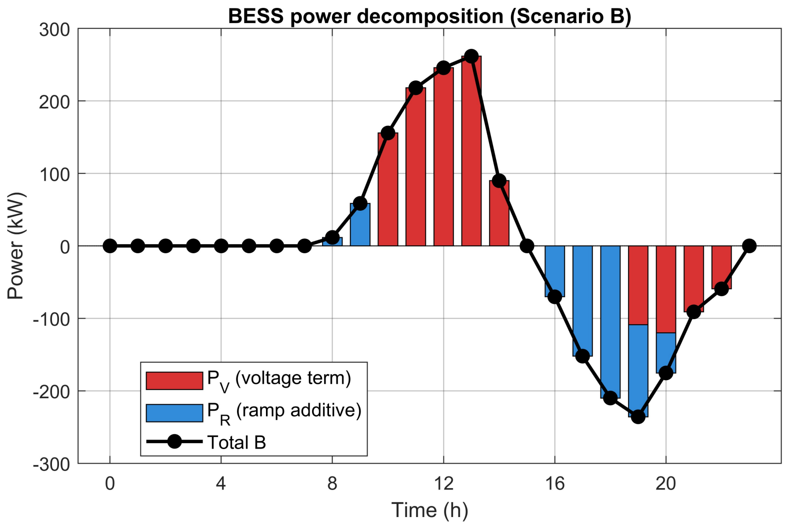

Figure 6. Decomposition of the battery energy storage system (BESS)) controls power into the voltage regulation component (P_v) and ramp-rate smoothing component (P_r).

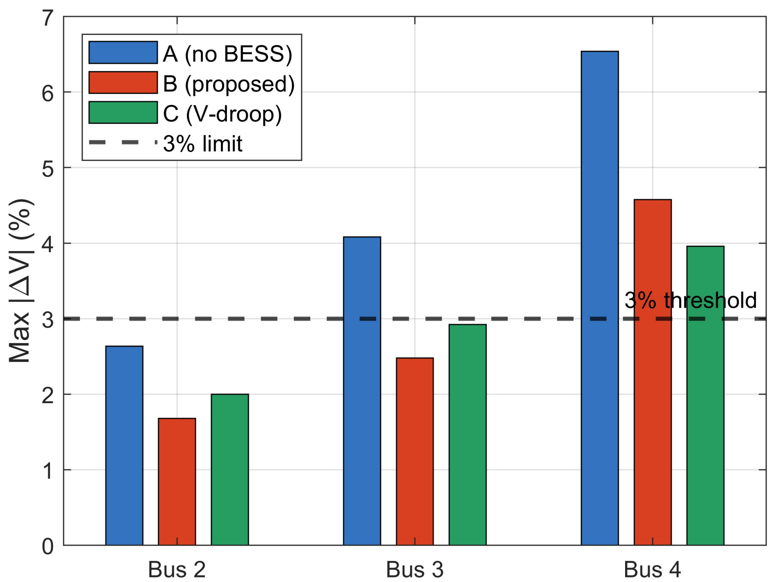

Figure 7. Maximum voltage deviation at load buses for Scenarios A, B, and C. Abbreviation: BESS: Battery energy storage system.

Table 5. Sensitivity analysis in the $\mathbf{k_v} \times \mathbf{RL}$ space

$\mathbf{k_v}$\RL	30	60	90	120
2,000	24/35/156	23/22/72	16/4/90	13/0/120
5,000	20/35/270	30/22/60	26/0/90	24/0/120
10,000	20/35/270	32/13/114	29/9/90	27/9/120
15,000	20/35/270	32/13/138	29/9/90	28/9/120

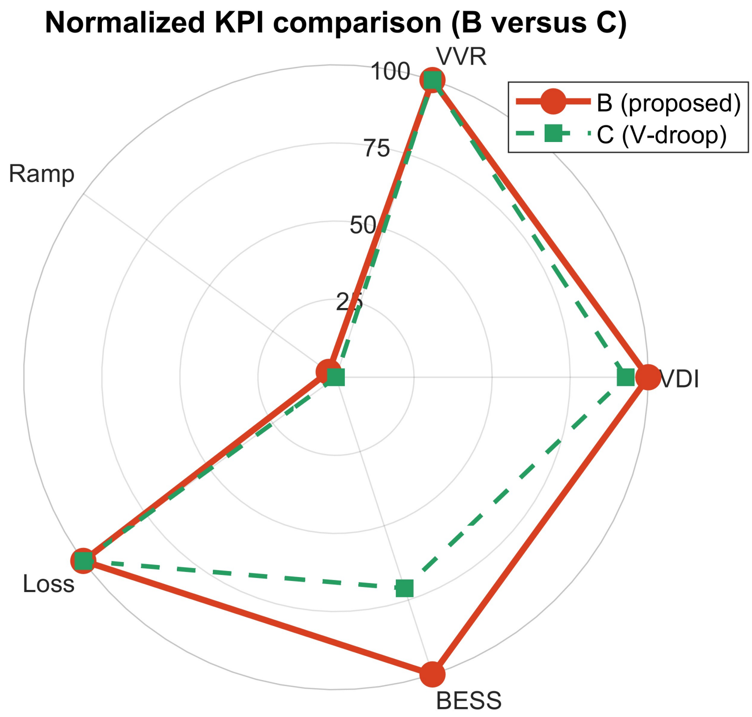

Figure 8. Radar chart of normalized key performance indicators (KPIs) for Scenarios B and C
Abbreviations: BESS: Battery energy storage system; VDI: Voltage deviation index; VVR: Voltage violation rate.

Table 6. Time-step resolution comparison (Δt = 1 h vs Δt = 5 min)

Metric	A (1h)	B (1h)	A (5min)	B (5min)
VDI_MA (pu)	0.02163	0.01327	0.02617	0.01709
VDI improvement (%)	—	38.66	—	34.67
RRV (%)	39.13	13.04	65.85	18.82
Max |ramp| (kW/h)	141.9	137.8	3,167.5	409.1
Mean |ramp| (kW/h)	54.4	35.4	162.8	49.5

Abbreviation: RRV: Ramp-rate violation rate; VDI: Voltage deviation index; VDI_MA: Mean absolute voltage deviation index.

Two quantitative results follow from **Table 6**: RRV_{NC} increases from 39.1% at $\Delta t = 1h$to 65.9% at $\Delta t = 5\,\text{min}$, while max $\mid \Delta P/\Delta t \mid_{NC} = 3,167.5kW/h \approx 22\times$ the hourly value, indicates that hourly sampling masks intra-hour cloud-induced ramps. Under Scenario B, the sub-hourly violation rate decreases from 65.9%to 18.8%, giving $\frac{65.9-18.8}{65.9} = 71.5\% \approx 72\%$ relative reduction; hence, the hierarchical controller preserves ramp-smoothing effectiveness at $\Delta t = 5\,\text{min}$, although the larger residual RRV reflects physically faster irradiance transients rather than controller degradation.

Figure 9 shows that the Markov cloud model generates high-frequency PV disturbances, with $P_{PV}^{\max} \approx 510kW$ and $\mid \Delta P_{PV} \mid > 300kW$ within several 5-min steps, which are filtered out when $\Delta t = 1h$. In **Figure 9B**, Scenario A violates the voltage deadband during 10–14h, with $V_{\max} \approx 1.058pu \lesssim 1.06pu$, and later drops to $V_{\min} \approx 0.953pu < V_{lo,db} = 0.97pu$. In contrast, Scenario B satisfies $V(t) \in [V_{lo,db}, V_{hi,db}] = [0.97, 1.03]pu$, with $V(t) \to 1.03pu$during PV peaks and $V(t) \to 0.97pu$in the evening. Therefore, $N_{viol,B} = 0$ at $\Delta t = 5\,\text{min}$, indicating that the convergence-from-zero inner loop provides sufficient sub-hourly response speed to absorb cloud-induced PV transients while maintaining voltage feasibility.

Figure 10 quantifies the sub-hourly ramp constraint as $\mid \Delta P_{PCC}/\Delta t \mid \leq 60kW/h$. In Scenario A, the uncontrolled ramp trajectory satisfies $\max \mid \Delta P_{PCC}/\Delta t \mid = 3,168kW/h$, with multiple excursions exceeding the plotted $\pm 500kW/h$range and $RRV_A = 65.9\%$. In Scenario B, the proposed controller reduces the peak ramp to $409kW/h$, giving a peak-reduction factor $3,168/409 \approx 7.7$, and lowers the violation rate to $RRV_B = 18.8\%$. Therefore, $\Delta RRV = (65.9 - 18.8)/65.9 = 71.5\% \approx 72\%$, confirming substantial sub-hourly ramp-smoothing improvement. The remaining spikes near $t \approx 8h$ occur when $\mid \Delta P_{PV} \mid$within one 5-min interval exceeds the feasible BESS correction, so the limiting factor becomes dispatch granularity $\Delta t = 5\,\text{min}$, not the hierarchical control law.

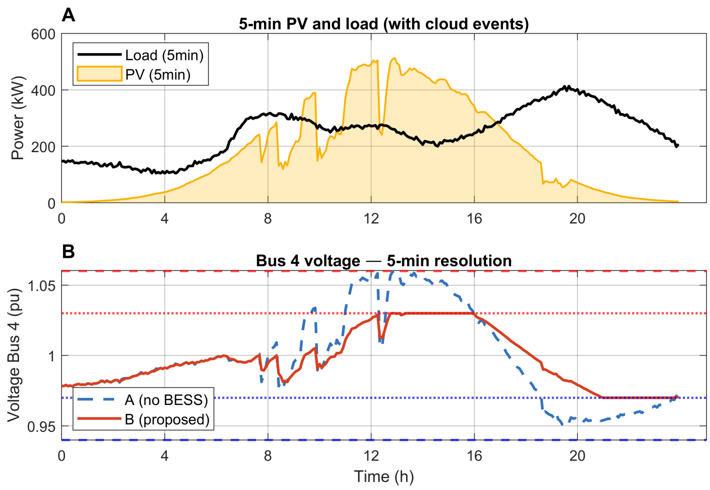

Figure 9. Five-minute resolution results: (A) PV/load with cloud events and (B) Bus 4 voltage trajectories for Scenarios A and B.
Abbreviations: BESS: Battery energy storage system; PV: Photovoltaic.

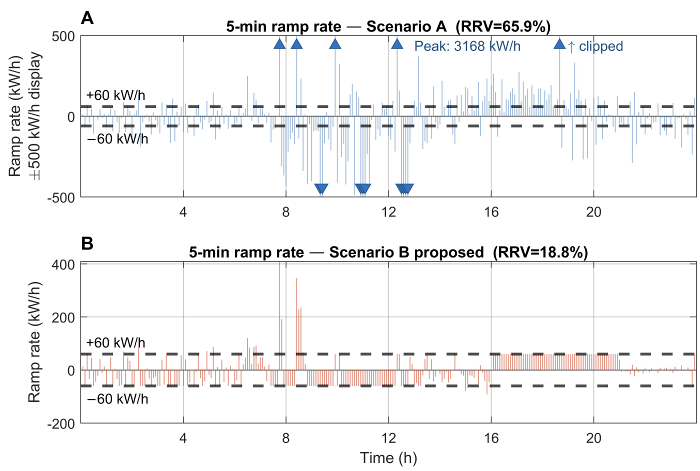

Figure 10. Five-minute resolution results: (A) PV/load with cloud events and (B) Bus 4 voltage trajectories for Scenarios A and B.
Abbreviations: BESS: Battery energy storage system; PV: Photovoltaic; RRV: Ramp-rate violation rate.

A formal scope limitation must be acknowledged: with $\Delta t = 1$ h, the simulation captures the energy-level behavior (SOC drift, throughput, integrated VDI) accurately, but underestimates the instantaneous PV ramp magnitudes. Empirical and simulation evidence suggests that peak ramps at $\Delta t = 1$ min can be 5–10× higher than at $\Delta t = 1$ h;[4] the 5-min assessment in **Table 6** already reveals a 22× amplification of maximum ramp magnitude. Consequently, the reported hourly RRV values are best interpreted as lower bounds, while the relative ranking among scenarios and the structural guarantees of the hierarchical algorithm remain valid across time resolutions.

4. Conclusion

This study proposed and validated a rule-based hierarchical BESS control algorithm for a low-voltage distribution network with a PV penetration level of 150%. The algorithm adopts a two-level priority architecture: voltage regulation (Level 1) and ramp-rate control (Level 2). The inner-loop mechanism converges from zero to determine the minimum charging/discharging power required for voltage compliance. The 24-hour simulation on a 4-bus CIGRE feeder with a $2,000$ kWh/300 kW community LFP BESS shows that the proposed algorithm reduces the mean voltage deviation index by 38.66% relative to the no-BESS scenario, while completely eliminating voltage violations, with VVR reduced from 2.8% to 0%. The ramp-rate violation rate decreases from 39.13% to 13.04%, with the mean ramp reduced by 34.9%. The network losses decrease by 41.57%. The SOC drift is only -1.8%, confirming the ability to maintain continuous energy balance over multiple operating days.

Compared with the single-objective droop scenario, the proposed algorithm is superior in all metrics: the VDI improvement is greater by 7.72 percentage points, the RRV is lower by 17.39 percentage points, the loss reduction is higher by 3.47 percentage points, and, most importantly, the SOC drift remains nearly neutral, whereas the droop case yields a drift of +30.3%.

The sensitivity analysis confirms that the algorithm remains stable over a wide parameter range $k_v \in [2,000,\ 15,000]\ kW/pu, R_L \in [30,\ 120]\ kW/h$ with a clear and controllable trade-off between VDI and RRV. The under-relaxation factor $\beta = 0.40$ guarantees monotonic convergence with $G_{eff} = 0.77 < 1$.

The algorithm has a simple rule-based structure. It does not require PV forecasting or load forecasting. It does not require solving an optimization problem. It is suitable for real-time implementation on embedded controllers for residential-scale community BESS applications. Future work includes extension to practical multi-branch distribution networks, integration of Volt-VAr reactive-power control, use of stochastic PV profiles, reduction of the simulation time step, and experimental validation through hardware-in-the-loop testing.

Acknowledgments

The author would like to gratefully acknowledge Electric Power University, Vietnam, for its support of this work.

Funding

None.

Conflict of interest

The author declares no conflicts of interest in this work.

Author contributions

This is a single-authored article.

Availability of data

Data are available from the corresponding author upon reasonable request.

AI tools statement

The author confirms that no AI tools were used in the preparation of this manuscript.

References

1. Alquthami T, Kumar RS, Shaikh AA. Mitigation of voltage rise due to high solar PV penetration in Saudi distribution network. *Electr Eng.* 2020;102(2):881-890. https://doi.org/10.1007/s00202-020-00920-z
2. Bueno-López M, Sanabria-Villamizar M, Molinas M, Alzate EB. Oscillation analysis of low-voltage distribution systems with high penetration of photovoltaic generation. *Electr Eng.* 2021;103(2):1141-1154. https://doi.org/10.1007/s00202-020-01152-x
3. Huo Y, Gruosso G. A novel ramp-rate control of grid-tied PV-battery systems to reduce required battery capacity. *Energy.* 2020;210:118433. https://doi.org/10.1016/j.energy.2020.118433
4. Lappalainen K, Wang GC, Kleissl J. Estimation of the largest expected photovoltaic power ramp rates. *Appl Energy.* 2020;278:115636. https://doi.org/10.1016/j.apenergy.2020.115636

5. European Committee for Electrotechnical Standardization (CENELEC). *EN 50160:2022, Voltage Characteristics of Electricity Supplied by Public Electricity Networks*. Brussels, Belgium: CENELEC; 2022.
6. IEEE Standards Association. IEEE Std 1547-2018 Standard for interconnection and interoperability of distributed energy resources with associated electric power systems interfaces. 2018. https://doi.org/10.1109/IEEESTD.2018.8332112
7. Khalil M, Elkhodragy TM, Salem WA. A novel hybrid algorithm based on optimal size and location of photovoltaic with battery energy storage systems for voltage stability enhancement. *Electr Eng*. 2025;107(1):1009-1034. https://doi.org/10.1007/s00202-024-02508-3
8. Yang J, Luo J, Zhang H. Fuzzy neural network based optimal and fair real power management for voltage security in distribution networks with high PV penetration. *J Electr Eng Technol*. 2020;15(6):2471-2478. https://doi.org/10.1007/s42835-020-00527-1
9. Shafiullah M, Ahmed SD, Al-Sulaiman FA. Grid integration challenges and solution strategies for solar PV systems: A review. *IEEE Access*. 2022;10:52233-52257. https://doi.org/10.1109/ACCESS.2022.3174555
10. Stecca M, Elizondo LR, Soeiro TB, Bauer P, Palensky P. A comprehensive review of the integration of battery energy storage systems into distribution networks. *IEEE Open J Ind Electron Soc*. 2020;1:46-65. https://doi.org/10.1109/OJIES.2020.2981832
11. Zhang Z, Mishra Y, Dou C, Yue D, Zhang B, Tian YC. Steady-state voltage regulation with reduced photovoltaic power curtailment. *IEEE J Photovolt*. 2020;10(6):1853-1863. https://doi.org/10.1109/JPHOTOV.2020.3026139
12. Nakamura M, Yoshizawa S, Ishii H, *et al*. Advanced voltage control method for improving the voltage quality of low-voltage distribution networks with photovoltaic penetrations. *Energy Inform*. 2021;4(S2):31. https://doi.org/10.1186/s42162-021-00149-5
13. Rezaei F, Esmaeili S. A bi-level inter-phase coordinated control method for voltage regulation in unbalanced LV distribution networks using PV-battery energy storage systems. *J Energy Storage*. 2024;101:113943. https://doi.org/10.1016/j.est.2024.113943
14. Zhao T, Parisio A, Milanović JV. Distributed control of battery energy storage systems in distribution networks for voltage regulation at transmission–distribution network interconnection points. *Control Eng Pract*. 2022;119:104988. https://doi.org/10.1016/j.conengprac.2021.104988
15. Lai T, Zhao H, Song Y, Wang L, Wang Y, He X. Mechanism and control strategies of lithium-ion battery safety: a review. *Small Methods*. 2024;9(1):2400029. https://doi.org/10.1002/smtd.202400029
16. Song Y, Wang L, Sheng L, *et al*. The significance of mitigating crosstalk in lithium-ion batteries: a review. *Energy Environ Sci*. 2023;16(5):1943-1963. https://doi.org/10.1039/D3EE00441D
17. Li H, Wang L, Song Y, Zhang Z, Zhang H, Du A, He X. Significance of current collectors for high performance conventional lithium-ion batteries: a review. *Adv Funct Mater*. 2023;33(49):2305515. https://doi.org/10.1002/adfm.202305515
18. Han Y, Luo J, Xie Y, Shen Y, Shao Z, Zhang Q. Dynamic Bridging Ligand-Induced Regulated Coordination Chemistry for Highly Reversible Zn-Metal Anodes. *Angew Chem Int Ed*. 2025;64(52):e12515. https://doi.org/10.1002/anie.202512515
19. Xu S, Xue Y, Chang L. Review of power system support functions for inverter-based distributed energy resources: Standards, control algorithms, and trends. *IEEE Open J Power Electron*. 2021;2:88-105. https://doi.org/10.1109/OJPEL.2021.3056627
20. Inaolaji A, Savasci A, Paudyal S. Distribution grid optimal power flow in unbalanced multiphase networks with Volt-VAr and Volt-Watt droop settings of smart inverters. *IEEE Trans Ind Appl*. 2022;58(5):5832-5843. https://doi.org/10.1109/TIA.2022.3181110
21. Chathurangi D, Jayatunga U, Perera S, Agalgaonkar A, Siyambalapitiya T. Comparative evaluation of solar PV hosting capacity enhancement using Volt-VAr and Volt-Watt control strategies. *Renew Energy*. 2021;177:1063-1075. https://doi.org/10.1016/j.renene.2021.06.037
22. Archetti JAG, Oliveira LW, Oliveira JG. Hardware-in-the-loop Volt–Watt and Volt–VAr control for distribution systems with high penetration of renewables. *J Control Autom Electr Syst*. 2023;34(1):177-188. https://doi.org/10.1007/s40313-022-00954-7
23. Carlak HF, Güler F. Power plant solar inverter control algorithm design for the Volt/VAr/demand control of a distribution network. *Electr Eng*. 2022;104(2):681-696. https://doi.org/10.1007/s00202-021-01317-2
24. Yousefi H, Gholamian SA, Zakariazadeh A. Voltage control approach based on PCPM distributed algorithm in the presence of high PV penetration: A stochastic modeling. *Electr Eng*. 2021;103(6):2561-2572. https://doi.org/10.1007/s00202-021-01249-x
25. Atif A, Khalid M. Savitzky–Golay filtering for solar power smoothing and ramp rate reduction based on controlled battery energy storage. *IEEE Access*. 2020;8:33806-33817. https://doi.org/10.1109/ACCESS.2020.2973036
26. Syed MA, Khalid M. Moving regression filtering with battery state of charge feedback control for solar PV firming and ramp rate curtailment.

IEEE Access. 2021;9:13198-13211.
https://doi.org/10.1109/ACCESS.2021.3052142

27. Abdalla AA, Moursi MSE, El-Fouly TH, Hosani KHA. A novel adaptive power smoothing approach for PV power plant with hybrid energy storage system. *IEEE Trans Sustain Energy*. 2023;14(3):1457-1473.
https://doi.org/10.1109/TSTE.2023.3236634
28. Hossain MB, Islam MR, Muttaqi KM, Sutanto D, Agalgaonkar AP. A compensation strategy for mitigating intermittencies within a PV powered microgrid using a hybrid multilevel energy storage system. *IEEE Trans Ind Appl*. 2023;59(4):5074-5086.
https://doi.org/10.1109/TIA.2023.3262771
29. Abdalla AA, Moursi MSE, El-Fouly THM, Hosani KHA. Reliant monotonic charging controllers for parallel-connected battery storage units to reduce PV power ramp rate and battery aging. *IEEE Trans Smart Grid*. 2023;14(6):4424-4438.
https://doi.org/10.1109/TSG.2023.3250987
30. Makibar A, Narvarte L, Lorenzo E. Contributions to the size reduction of a battery used for PV power ramp rate control. *Sol Energy*. 2021;230:435-448.
https://doi.org/10.1016/j.solener.2021.10.047
31. Ryu A, Ishii H, Hayashi Y. Battery smoothing control for photovoltaic system using short-term forecast with total sky images. *Electr Power Syst Res*. 2021;190:106645.
https://doi.org/10.1016/j.epsr.2020.106645
32. Cano A, Arévalo P, Benavides D, Jurado F. Comparative analysis of HESS (battery/supercapacitor) for power smoothing of PV/HKT, simulation and experimental analysis. *J Power Sources*. 2022;549:232137.
https://doi.org/10.1016/j.jpowsour.2022.232137
33. Bektaş E, Bayındır KÇ, Terciyanlı A, Aydın RA, Baykal Ş, Yılmaz H. Energy management integrated Volt-VAr optimization for distribution systems with SVR, PV inverter, and BESS: A case study in distribution system of Elazığ/Turkey. *Electr Eng*. 2022;105(2):663-680.
https://doi.org/10.1007/s00202-022-01690-6
34. Kumar JS, Kumar N. Optimal scheduling of grid connected solar photovoltaic and battery storage system considering degradation cost of battery. *Iran J Sci Technol Trans Electr Eng*. 2022;46(4):1175-1188.
https://doi.org/10.1007/s40998-022-00529-x
35. Zakaria S, Mativenga P, Cseke A. Energy consumption and scope 2 emissions for fused deposition modelling. *Procedia CIRP*. 2022;105:31-36.
https://doi.org/10.1016/j.procir.2022.02.006
36. Emarati M, Barani M, Farahmand H, Aghaei J, Del Granado PC. A two-level over-voltage control strategy in distribution networks with high PV penetration. *Int J Electr Power Energy Syst*. 2021;130:106763.
https://doi.org/10.1016/j.ijepes.2021.106763
37. Khan HA, Zuhaib M, Rihan M. Voltage fluctuation mitigation with coordinated OLTC and energy storage control in high PV penetrating distribution network. *Electr Power Syst Res*. 2022;208:107924.
https://doi.org/10.1016/j.epsr.2022.107924
38. López L, Ropero IL, Gómez-Cornejo J, Aranzabal I, Eguía P. Analysis of impact for PV-BES strategies in low-voltage distribution system. *Electr Eng*. 2025;107(2):2147-2162.
https://doi.org/10.1007/s00202-024-02620-4
39. Fahad S, Goudarzi A, Xiang J. Demand management of active distribution network using coordination of virtual synchronous generators. *IEEE Trans Sustain Energy*. 2021;12(1):250-261.
https://doi.org/10.1109/TSTE.2020.2990917
40. Mohamed AA, Jun M, Mahmud R, *et al*. Hierarchical control of megawatt-scale charging stations for electric trucks with distributed energy resources. *IEEE Trans Transp Electrif*. 2023;9(4):4951-4963.
https://doi.org/10.1109/TTE.2022.3167647
41. Nguyen M-C. Coordinated demand-side management and energy storage system for a hybrid photovoltaic–wind microgrid under time-of-use tariffs. *An Int J Optim Control: Theor Appl*. 2026;16(2):566-579.
https://doi.org/10.36922/IJOCTA025480217
42. Demirtas M, Ahmad F. Fractional fuzzy PI controller using particle swarm optimization to improve power factor by boost converter. *An Int J Optim Control: Theor Appl*. 2023;13(2):205-213.
https://doi.org/10.11121/ijocta.2023.1260
43. Perin D, Karaoglan AD, Yilmaz K. Rotor design optimization of a 4000 rpm permanent magnet synchronous generator using moth flame optimization algorithm. *An Int J Optim Control: Theor Appl*. 2024;14(2):123-133.
https://doi.org/10.11121/ijocta.1407
44. Patari N, Venkataramanan V, Srivastava A, Molzahn DK, Li N, Annaswamy A. Distributed optimization in distribution systems: Use cases, limitations, and research needs. *IEEE Trans Power Syst*. 2022;37(5):3469-3481.
https://doi.org/10.1109/TPWRS.2021.3132348
45. Zhang Q, Guo Y, Wang Z, Bu F. Distributed optimal conservation voltage reduction in integrated primary-secondary distribution systems. *IEEE Trans Smart Grid*. 2021;12(5):3889-3900.
https://doi.org/10.1109/TSG.2021.3088010
46. Paudel A, Khorasany M, Gooi HB. Decentralized local energy trading in microgrids with voltage management. *IEEE Trans Ind Inform*. 2021;17(2):1111-1121.
https://doi.org/10.1109/TII.2020.2980160
47. Montoya OD, Arias-Londoño A, Garrido V, Gil-González W, Grisales-Noreña LF. A quadratic convex approximation for optimal operation of battery energy storage systems in DC distribution networks. *Energy Syst*. 2021;14:985-1005.
https://doi.org/10.1007/s12667-021-00495-z

48. Jamroen C. The effect of SoC management on economic performance for battery energy storage system in providing voltage regulation in distribution networks. *Electr Power Syst Res.* 2022;211:108340. https://doi.org/10.1016/j.epsr.2022.108340
49. Gräf D, Marschewski J, Ibing L, *et al.* What drives capacity degradation in utility-scale battery energy storage systems? The impact of operating strategy and temperature in different grid applications. *J Energy Storage.* 2022;47:103533. https://doi.org/10.1016/j.est.2021.103533
50. Hupez M, Toubeau J-F, De Grève Z, Vallée F. A new cooperative framework for a fair and cost-optimal allocation of resources within a low voltage electricity community. *IEEE Trans Smart Grid.* 2021;12(3):2201-2211. https://doi.org/10.1109/TSG.2020.3040086
51. Jouttijärvi S, Karttunen L, Ranta S, Miettunen K. Techno-economic analysis on optimizing the value of photovoltaic electricity in a high-latitude location. *Appl Energy.* 2024;361:122924. https://doi.org/10.1016/j.apenergy.2024.122924
52. Open Power System Data. Data package time series, version 2020-10-06. 2020. https://doi.org/10.25832/time_series/2020-10-06

Thanh Ngo Ngoc *received his Ph.D. degree in Control and Automation Engineering from the Institute of Information Technology, Viet Nam, 2020. He is currently a lecturer in the Faculty of Information Technology, Electric Power University, Hanoi, Vietnam. His research interests encompass the optimization of energy systems, distributed generation, renewable and solar energy engineering, as well as the application of intelligent techniques to the control of distributed power grids.*

https://orcid.org/0009-0009-1914-3726

An International Journal of Optimization and Control: Theories & Applications (https://accscience.com/journal/ijocta)

This work is licensed under a Creative Commons Attribution 4.0 International License. The authors retain ownership of the copyright for their article, but they allow anyone to download, reuse, reprint, modify, distribute, and/or copy articles in IJOCTA, so long as the original authors and source are credited. To see the complete license contents, please visit http://creativecommons.org/licenses/by/4.0/.